Supplementary Information

Artificial Water Channels Enable Fast and Selective Water Permeation Through Water-Wire Networks

Woochul Song, Himanshu Joshi, Ratul Chowdhury, Joseph S. Najem, Yue-xiao Shen, Chao Lang, Codey B. Henderson, Yu-Ming Tu, Megan Farell, Megan E. Pitz, Costas D. Maranas, Paul S. Cremer, Robert J. Hickey, Stephen A. Sarles, Jun-li Hou, Aleksei Aksimentiev, and Manish Kumar

Supplementary methods and discussions

Synthesis of PAH[4] channels

PAH[4]s were synthesized in two steps: synthesis of hybrid[4]arene macrocycles followed by appending of phenylalanine tripeptide (D-Phe-L-Phe-D-Phe-COOH, triPhe) side chains on hybrid[4]arene macrocycles, respectively (Supplementary Fig. 1). Each step followed reported procedures which were first proposed by Boinski *et al*.[1] and Chen *et al*.[2], respectively resulting in a new molecule which we term peptide-appended hybrid[4]arene, PAH[4]. Hybrid[4]arenes were employed as building templates due to following structural features. First, hybrid[4]arene macromolecule has central a cavity structure with desirable size dimensions around ~3Å to ~5Å (Supplementary Fig. 1). Second, they have eight aromatic hydroxide reactive groups of which four face one direction (say upward) and others face downward. This bidirectional feature is important to form cylinder-like transmembrane structures when triPhe chains are extended on these reactive groups. Lastly, hybrid[4]arenes have asymmetric and slightly kinked conformation that is advantageous in terms of possibly conferring additional free void fractions in the membranes and thereby enhancing structural flexibility of PAH[4]s and water permeability. The triPhe chains were selected as a scaffold to construct cylinder-like channel backbones, based on our previous study on peptide-appended pillar[5]arene (PAP[5]), an AWC which is structurally analogous to PAH[4] (Supplementary Fig. 2)[3,4]. Proton nuclear magnetic resonance spectroscopy (^{1}H-NMR) and inductively coupled plasma mass spectrometry (ICP-MS) spectra of prepared PAH[4]s are shown in Supplementary Fig. 3 and 4, respectively.

8-hydroxypyrene-1,3,6-trisulfonic acid (HPTS) dye assay for Na^+ permeation test

HPTS dyes have been widely used to study molecular transport of ions through vesicles in a qualitative manner[5-7]. Lipid vesicles were prepared with HPTS-containing rehydration buffer (10 mM HEPES, 1 mM HPTS, 100 mM NaCl, 0.01% (w/v) NaN_3 at pH 7.0). After vesicle extrusion, HPTS-encapsulating vesicles were purified using Sephadex G-50 resin columns to remove free HPTS dyes. 50 μL of vesicle solutions was rapidly mixed with 1.95 mL of buffer (10 mM HEPES, 1 mM HPTS, 100 mM NaCl, 0.01% (w/v) NaN_3 at pH 8.0) and fluoresce intensity change was monitored for five minutes using SpectraMax M5 microplate reader (Molecular Devices). After five minutes of measurements, 25 μL of 20 % (v/v) Triton X-100 was added to completely lyse lipid vesicles and release entrapped HPTS dyes into buffer solution. For PAH[4] channels, mCLR 0.005 vesicles were used for the HPTS assay. Gramicidin A (gA), which is well known cation transport pore-forming peptide channel, was used as a positive control of cation (Na^+) transport. The same molar amount of gAs with tested PAH[4]s was dissolved in buffer before vesicle solution addition, followed by same procedure of measuring fluorescence intensity change.

Definition of water permeability units used in this article

There are a variety of permeability units currently used in membrane biophysics and synthetic membrane science and engineering literature. This could be a source of confusion. Since this paper attempts to synthesize and present knowledge and data that combine both fields, this section was put together to clarify the common definitions used in the two fields as used in this work. Water

permeability of biological membranes (e.g., lipid vesicular membranes) is commonly expressed using the osmotic permeability (coefficient) term (P_f, cm·s^{-1}) as shown in equation (1).

$$j_w = P_f \, \Delta C_{osm} \quad (1)$$

where j_w is mole flux of water (mole·m^{-2}·s^{-1}), P_f is osmotic water permeability coefficient (cm·s^{-1}), and ΔC_{osm} is the osmolarity difference across the membrane (mol·L^{-1}). The equation (1) has a similar formula with salt permeability which is also commonly used in synthetic membrane research field, the so called "B" value (2).

$$j_s = B \, \Delta C_s \qquad (2)$$

where j_s is mole flux of salt (mol·m^{-2}·s^{-1}), B is salt permeability coefficient (cm·s^{-1}), and ΔC_s is the salt concentration difference across the membrane (mol·L^{-1}). Both the osmotic water permeability (P_f , cm·s^{-1}) and salt permeability (B, cm·s^{-1}) describe molecular transport behavior across membranes via the solution-diffusion mechanism driven by molar concentration gradients, and these values are correlated with intrinsic water and salt permeability as shown in equation (3) and (4), respectively.

$$j_w = P_f \Delta C_{osm} = \frac{P_w}{L} \Delta C_{osm} \qquad (3)$$

$$j_s = B \Delta C_s = \frac{P_s}{L} \Delta C_s \qquad (4)$$

where P_w and P_s are intrinsic water and salt permeability, respectively, which have same units of diffusivity (cm^2·s^{-1}), and L is the thickness of membranes.

Single channel osmotic permeability is similarly defined with P_f as shown in equation (5).

$$j_{w,chan} = P_{f,chan} \, \Delta C_{osm} \quad (5)$$

where $J_{w,chan}$ is mole flux of water through single channel (mol·s^{-1}), $P_{f,chan}$ is single channel osmotic water permeability (cm^3·s^{-1}), and ΔC_{osm} is the osmolarity difference across the membrane (mol·L^{-1} or osmol·L^{-1}). Note that, single channel osmotic permeability ($P_{f,chan}$, cm^3·s^{-1}) does not take into account the cross-sectional area of channels occupied in membranes and has different unit with that of membranes' permeability (P_f, cm·s^{-1}) in equation (1). This value has also been widely reported using a unit of number of H_2O molecules per second (H_2O·s^{-1}), by multiplying $P_{f,chan}$ (cm^3·s^{-1}) with the molar volume of water and the Avogadro's number.

In the synthetic membrane research field, the productivity of membranes has been presented using "A" value which describes volumetric water permeance (6).

$$J_{w,mem} = A \, (\Delta P - \Delta \pi) \quad (6)$$

where $J_{w,mem}$ is volumetric water flux of membrane (L·m^{-2}·hour^{-1}), A is hydraulic water permeability (L·m^{-2}·hour^{-1}·bar^{-1}), and ΔP and $\Delta \pi$ are hydraulic and osmotic pressure differences across the membranes (bar^{-1}), respectively. As shown in equation (1) and (6), routinely used water permeability values used in biophysical literature (P_f, cm·s^{-1}) and synthetic membrane literature (A,

$L \cdot m^{-2} \cdot hour^{-1} \cdot bar^{-1}$) have different unit dimensions and, are therefore, difficult to compare against each other.

The Van't Hoff equation, combined with equation (1), enables us to correlate the osmotic water permeability (coefficient) of biological membranes to pressure normalized volumetric water flux (A_{osm}) as shown in equation (7) and (8).

$$J_w = j_w v_w = v_w P_f \Delta C_{osm} = v_w P_f \frac{\Delta\pi}{RT} \qquad (7)$$

$$A_{osm} = \frac{J_w}{\Delta\pi} = \frac{P_f v_w}{RT} \qquad (8)$$

where J_w and j_w are volumetric ($L \cdot m^{-2} \cdot s^{-1}$) and mole ($mole \cdot m^{-2} \cdot s^{-1}$) flux of water, respectively, v_w is the partial molar volume of water, ΔC_{osm} is the osmolarity difference, $\Delta\pi$ is osmotic pressure, R is the ideal gas constant, and T is temperature. Now, A_{osm} has a same dimension (volumetric water flux normalized by pressure) with "A" value and, therefore, it can be readily compared to water permeability coefficient of traditional polymeric membranes. To avoid any confusion, all water permeability in this Supplementary Material document is followed by unit information in parenthesis for clarity.

Water permeability calculation based on recently proposed osmotic permeability equation

While equation (1) in the main text is one of most widely adapted model to calculate vesicular membranes' water permeability based on stopped-flow scattering experiments, Pohl and coworkers recently proposed a corrected version of this equation in order to more accurately quantify water permeability of vesicular membranes, as shown in equation (9)[8,9].

$$P_f(m \cdot s^{-1}) = \frac{k}{(S/V_0) \times v_w} \times \frac{C_{in,0} + C_{out}}{2{C_{out}}^2} \qquad (9)$$

where $C_{in,0}$ and C_{out} are osmolyte concentration inside (initial, t = 0) and outside of vesicles, respectively.

PAH[4] cluster size estimation based on lateral diffusivity of channels measured by FRAP

Lateral diffusivity of TR-DHPE ($D_{lat,DHPE}$) and PAH[4] channels ($D_{lat,PAH[4]}$) were measured as 0.67 (±0.03) $\mu m^2/s$ and 0.41 (±0.17) $\mu m^2/s$, respectively (Supplementary Fig. 13). Notably, fluorescence recovery of PAH[4]-reconstituted membranes demonstrates lateral diffusion of PAH[4] channels in lipid bilayer membranes. Slow diffusivity of TR-DHPE is attributed to hindered diffusion caused by channel aggregation. Using the $D_{lat,DHPE}$, the lipid membrane viscosity (μ_m) could be calculated from the Saffman-Delbrück equations of (10) and (11)[10].

$$D_{lat} = \frac{k_B T}{4\pi\mu_m h}[\ln(2L_{sd}/a) - \gamma] \quad (10)$$

$$L_{sd} = \frac{h\mu_m}{2\mu_f} \quad (11)$$

where k_B is the Boltzmann constant, T is the temperature (K), h is the height of the membranes, a is radius of cross-sectional area of diffusing molecules (domains) in the membranes, γ is the Euler-

Mascheroni constant (≈0.577), L_{sd} is the Saffman-Delbrück length, and μ_f is bulk fluid viscosity (water). From this, the μ_m of PAH[4]-reconstituted PC/PS lipid membranes could be calculated as ~0.62 Pa·s.

Due to the limited condition of equation (11) ($a \ll L_{sd}$), an analytical solution of translational diffusivity in lipid membranes was used to estimate the PAH[4] channel aggregation sizes, as shown in equation (12)[11,12].

$$D_{lat} = \frac{k_B T}{4\pi\mu_m h}[\ln(2/\epsilon) - \gamma + 4\epsilon/\pi - (\epsilon^2/2)\ln(2/\epsilon)][1 - (\epsilon^3/\pi)\ln(2/\epsilon) + c_1\epsilon^{b_1}/(1 + c_2\epsilon^{b_2})]^{-1} \quad (12)$$

where $\epsilon = a/L_{sd}$, $b_1 = 2.74819$, $b_2 = 0.51465$, $c_1 = 0.73761$, and $c_2 = 0.52119$. As a result, the size of PAH[4] clusters in lipid bilayer is estimated to be ~150 nm in diameter on average, while showing broad size distribution from ~50 nm to ~900 nm.

Thermodynamic calculation of single channel water permeability based on activation energy

Pohl and coworkers recently described an approach to correlate channel water permeability and activation energy (E_a) of single file water permeation through channels[13]. It describes that, when single-file water permeation occurs, a common characteristic in biological and biomimetic channels, single channel permeability should be thermodynamically correlated with E_a of water permeation as equation (13).

$$P_{f,E_a}(cm^3 \cdot s^{-1}) = \frac{v_0 v_w}{N_A}\exp\left(\frac{-E_a}{k_B T}\right) \quad (13)$$

where P_{f,E_a} is calculated single channel water permeability ($cm^3 \cdot s^{-1}$), v_0 is the universal transition state theory attempt frequency (~10^{13} s^{-1}), v_w is molar volume of water, N_A is the Avogadro's constant, k_B is the Boltzmann constant, and T is temperature (K). Correspondence between osmotic single channel permeability (P_f, $cm^3 \cdot s^{-1}$) obtained from experiments and calculated permeability (P_{f,E_a}, $cm^3 \cdot s^{-1}$) confirms reliability of evaluated permeability values.

Analysis details of using colloidal quenching dyes for intrinsic ion permeability measurement

A series of colloidal dyes are known to have a specific collisional fluorescence quenching mechanism which is described by the Stern-Volmer equation (14)[14,15].

$$\frac{F_0}{F} - 1 = K_{sv}[Q] \quad (14)$$

where F_0 is fluorescence intensity of the dyes under quencher-free environment, F is fluorescence intensity with presence of quenchers, K_{sv} is the Stern-Volmer constant, and $[Q]$ is molar concentration of quenchers. First derivative of equation (14) with respect to time becomes equation (15).

$$\left.\frac{d[Q]}{dt}\right|_{t=0} = \frac{-1}{K_{sv}F_0}\left.\frac{dF}{dt}\right|_{t=0} \quad (15)$$

The equation (15) points out that fluorescence intensity change of colloidal quenching dyes can be

used to quantitatively trace time-dependent concentration change of quenchers in the system. Hence, we used this equation to measure Cl^- concentration change inside lipid vesicles after abruptly exposing the vesicles to higher Cl^- concentration environments in a stopped-flow instrument and used this information to calculate quantitative Cl^- flux across vesicular membranes at different Cl^- concentration gradient conditions.

Among commercially available halide ion sensitive colloidal quenching dyes, lucigenin dyes have the highest K_{sv} value (390 M^{-1} for Cl^- at bulk solution phase) and are most sensitive to Cl^- ion concentration change in aqueous systems[15]. Therefore, lucigenin dyes were selected as measurement probes. The K_{sv} value inside vesicular environments (inside ~200 nm lipid vesicles) was first determined using a SpectraMax i3x microplate reader (Molecular Devices). Control lipid vesicles encapsulating lucigenin dyes were prepared using the same film rehydration method as described previously with the exception of using lucigenin-containing and Cl^- free rehydration buffer (10 mM HEPES, 1 mM lucigenin, 100 mM KNO_3, and 0.01% NaN_3 at pH 7.0) for the rehydration step. Note that NO_3^- ions were used as counter ions of Cl^- for balancing osmotic pressure across the vesicular membranes for these stopped-flow experiments. After extrusion, vesicles were purified with Sephadex G-50 size exclusion resin columns (Sigma Aldrich) to separate lucigenin-encapsulating vesicles from extravesicular free lucigenin dyes. Prepared vesicles were mixed with different Cl^- concentration buffers and their fluorescence intensities (455 nm excitation and 505 nm emission) were monitored until the systems were equilibrated via Cl^- diffusion through vesicular membranes for 20 hours (Supplementary Fig. 15). Plotting of equation (14) (Stern-Volmer plot) presents that intravesicular environments were equilibrated after ~12 hours and the K_{sv} value inside the vesicles could be obtained from the slope of this plot after 12 hours (Supplementary Fig. 15).

Calculation of intrinsic water and salt (NaCl) permeability values of PAH[4] channel

The area of biomimetic and biomimetic membranes could benefit from quantitatively descriptive intrinsic water and salt permeability of biomimetic channels and membranes built around them, as it will provide a uniform scientific criterion to develop membrane platforms and compare it to existing desalination processes[16,17]. Water and salt permeabilities of nonporous desalination membranes are commonly described by equations (16) and (17)[16].

$$P_w = K_w \times D_w \quad (16)$$

$$P_s = K_s \times D_s \quad (17)$$

where P_w and P_s are intrinsic water and solute permeabilities ($cm^2 \cdot s^{-1}$), K_w and K_s are water and solute partition coefficients for the selected membrane, and D_w and D_s are water and solute diffusion coefficients ($cm^2 \cdot s^{-1}$) of water and salt in the selected membrane, respectively. Water/salt selectivity (P_w/P_s) is defined as a permeability ratio between water and salt as equation (18).

$$\frac{P_w}{P_s} = \frac{K_w}{K_s} \times \frac{D_w}{D_s} \quad (18)$$

where K_w/K_s and D_w/D_s are solubility selectivity and diffusivity selectivity, respectively. Enhancing both permeability and selectivity and overcoming the so called “upper bound limit of

permselectivity" for current membranes is the goal of most membrane research and development efforts.

Diffusion coefficient of water molecules inside water channels ($D_{w,chan}$) has been defined differently from D_w. For example, due to the characteristic water transport feature inside molecularly constricted channel environments where transport takes place via a single file of water molecuels, continuum theories are not applicable. Therefore, the Einstein relation has been used to describe water molecules' transport behavior permeating through water channels (19)[8,18-20].

$$D_{w,chan}(cm^2 \cdot s^{-1}) = \frac{k_0 z^2}{2} = \frac{z^2 P_{f,chan}(cm^3 \cdot s^{-1})}{2v_w} \quad (19)$$

where k_0 is the transport rate, z is the average distance between two water molecules in a row inside single-file permeation region, v_w is the molecular volume of one water molecule, and $P_{f,chan}$ is single channel permeability ($cm^3 \cdot s^{-1}$). Note that, as seen in equation (19), $D_{w,chan}$ does not take into account the entire channel area occupied in membranes but just considers cross-sectional area occupied by single water molecules. It implies that, from the membrane engineering perspective, direct comparison of $D_{w,chan}$ (channel) to D_w (membrane) could lead to a biased overestimation of water channels' potential for membrane applications. Due to similar reasons, knowledge gaps in comparing solubility parameters (solubility and solubility selectivity) of channels to that of membranes still remain.

Even though it is difficult to consider solubility and diffusivity parameters of both channels and membranes separately, intrinsic permeability can be readily calculated from experimental results, taking into account the previously stated challenges [21]. As shown in equation (3) and (4), vesicular membranes' intrinsic water and salt permeability can be expressed as equation (20) and (21).

$$P_w = P_f \, L \qquad (20)$$

$$P_s = B \, L \qquad (21)$$

where P_w and P_s are intrinsic water and salt permeability ($cm^2 \cdot s^{-1}$), respectively, P_f is the osmotic water permeability ($cm \cdot s^{-1}$), B is salt permeability ($cm \cdot s^{-1}$) and L is the thickness of the membranes. Similarly, single channels' intrinsic water and salt permeability can be obtained by taking account the cross-sectional area of channels occupied in the membranes (22) and (23).

$$P_{w,chan} = \frac{P_{f,chan}}{a_{chan}} \, L \qquad (22)$$

$$P_{s,chan} = \frac{B_{Cl,chan}}{a_{chan}} \, L \qquad (23)$$

where $P_{w,chan}$ and $P_{s,chan}$ are intrinsic water and salt permeability of channels ($cm^2 \cdot s^{-1}$), respectively, $P_{f,chan}$ is single channel osmotic permeability ($cm^3 \cdot s^{-1}$), $B_{Cl,chan}$ is single channel salt (chloride) permeability ($cm^3 \cdot s^{-1}$) which is shown in equation (11) in the main text, L is the thickness of the membranes, and a_{chan} is cross-sectional area of channels in the membranes (m^2). a_{chan} was

observed as ~2 nm^2 from long-time scale (~400 ns) MD simulations.

The intrinsic water and salt permeability of PAH[4]-integrated biomimetic membranes with different channel areal fractions (α) were calculated based on each permeability value of PAH[4] channels and biomimetic membrane matrices. Since all permeability values are already normalized by membrane area and thickness, intrinsic permeability of channel-integrated membranes could be readily calculated as seen in equation (24) and (25).

$$P_{w,\alpha} = (1-\alpha)\, P_{w,BBM} + \alpha\, P_{w,chan} \qquad (24)$$

$$P_{s,\alpha} = (1-\alpha)\, P_{s,BBM} + \alpha\, P_{s,chan} \qquad (25)$$

where $P_{w,\alpha}$ and $P_{s,\alpha}$ are water and salt permeability ($cm^2 \cdot s^{-1}$) of channel-integrated biomimetic membranes of which fractional area (α) is occupied by channels, $P_{w,BBM}$ and $P_{s,BBM}$ are water and salt permeability of biomimetic membrane matrices, and $P_{w,chan}$ and $P_{s,chan}$ are water and salt permeability of channel, respectively.

In-silico experiments: generation of representative PAH[4] cluster configurations

A PAH[4] monomeric channel was built by *in silico* sculpting eight triPhe chains to the crystal structure of hybrid[4]arene, crystallized by Boinski *et al*.[1]. To create the atomistic model of PAH[4] molecule, we added eight phenylalanine tripeptides chains to the pdb of hybrid[4]arene molecule using the VMD software[22]. The parameters for the non-standard hybrid[4]molecule connected with one phenylalanine peptide to each of the eight arms, as shown in green color in Supplementary Fig. 22a, were generated using the CHARMM general force fields (CGenFF) webserver[23]. CHARMM36 force-field[24] was used to describe the the remaining phenylalanine side chains. Note that, since myriad cluster configurations could be possible based on several factors such as the number of PAH[4]s and inter-facing directions due to the asymmetric PAH[4] structure (Supplementary Fig. 1), we performed *in silico* "oligomerization" experiments[25,26] and generated three possible representative cluster configurations, which are composed of 22 PAH[4] molecules (22-cluster) evolved from energy-minimized PAH[4] dimer structures, and termed them as lateral, orthogonal, and inverted cluster configurations, respectively (Supplementary Fig. 19 and 20). The PAH[4] channel was CHARMM minimized after building appropriate force-field parameter and topology files. Additional solvation parameters were also added to facilitate the incorporation of an implicit solvation term (using generalized Born solvation) along with van der Waals, and electrostatic energies for the channel. In order to discern thermodynamically stable dimeric geometries, we performed a simulated-annealing based lateral docking of one monomer against another similar or a flipped monomer and explored six possible configurations (Supplementary Fig. 19)[25]. Based on the free energies of dimerization, which were computed using the 'interaction-energy' plugin developed in a previous work that reflect the sum of free energies associated with van der Waals, electrostatics, and solvation terms computed at the binding interface [25], only three configurations were identified to have negative free energies and hence stable. We call these three geometries as (a) lateral – where the ~3 Å side of two dimers are next to each other, (b) inverted – where the ~3 Å side of one normal and one flipped monomer are next to each other, and (c) orthogonal – where the ~5 Å side of two channels are juxtaposed (Supplementary Fig. 19 and 20).

A phosphatidyl choline (POPC)-based membrane patch was used to immobilize 25 such dimers of each type in three independent molecular dynamics (MD) simulation setups. Each of these 400 ns simulations (with Na^+ and Cl^- ions) provided vital insights about water permeation rates and ion rejection (Supplementary Fig. 21). Results from MD revealed much lower water permeation rates than observed in experiments at high channel density region (Fig. 2b). We hypothesized that possible oligomerization of these dimers facilitate high water transport based on their tendency to aggregate as seen from the last 30 ns of the MD simulations as well as from the experiments (FRAP, AFM, and enhancing permeability at high channel density) (Fig. 2b, Supplementary Fig. 12 and 13). Out of the 25 dimers from each of the three setups, we isolated the one which exhibited the highest water transport rates during the course of MD trajectory. Thereafter, we used these three structures to obtain three separate CHARMM-minimized oligomeric cluster (or bouquet) configurations (Supplementary Fig. 19 and 20). The bouquet-generation protocol involved iterative docking of PAH[4] dimers onto a growing cluster followed by subsequent short energy minimization run (1000 CHARMM iterations) of the new cluster. This yielded three thermodynamically stable clusters, one for each dimer geometry. Each of the three stable configurations comprised 11 lateral, inverted, and orthogonal dimers respectively. Structural inspection of the cluster structures revealed that the inverted and orthogonal geometries had room for conformational flexibility at the four corners of the clusters, which could lead to defects (pinholes) at the cluster-membrane interface (Supplementary Fig. 19). If these defects are comparable or bigger than the size of a water molecule, they would render the assessment of water permeation rates inaccurate. To mitigate this, we added one monomer of the respective type at each corner that were able to stabilize them. We further performed detailed energy-minimization (of 100,000 CHARMM iterations) with first 5,000 steps of gradient descent followed by 95,000 adoptive-bases Newton Raphson minimization steps on these clusters that yielded stable elliptical geometries, which are easy to embed in membranes without leaving any defects. Thus, each of the three resulting cluster configurations were constituted of 11 dimers of the respective type, and four extra monomers for the inverted and orthogonal cases. The oligomerized clusters now presented the water permeating paths cooperatively interconnected between channels. Nonetheless, to ensure an identical MD analysis of water permeation through these clusters, we replaced the four monomers in the two aforementioned geometries with the amphiphilic membrane patch to eliminate pinholes. Thus, all three resultant clusters had exactly 11 dimers. A 400 ns all-atom MD simulation was performed using the cluster-membrane assembly and the water permeation rates and ion rejection performances were determined.

Molecular dynamics (MD) simulations

To elucidate the microscopic mechanism of transmembrane water permeation through the PAH[4] channels, we have performed atomistic molecular dynamics (MD) simulations. Using a design method similar to that previously applied to PAP[5] channels[3], we built an atomistic model of the PAH[4] channel (Supplementary Fig. 1 and Supplementary Video 1). To characterize their nanoscale structure and dynamics, we created the all-atom models of PAH[4] channels in various conformations (monomer, dimer and 11-dimer cluster), embedded them into a patch of pre-equilibrated 1-palmitoyl-2-oleoyl-sn-glycero-3-phosphatidylcholine (POPC) lipid bilayer membrane and solvated in 0.6 M NaCl solution.

First, we simulated a system of 25 PAH[4] monomers arranged as a regular array in the lipid bilayer membrane (Supplementary Fig. 22a,b). We constrained the non-hydrogen atoms of the PAH[4] to their initial potions for the first 5 ns of the MD simulation and subsequently carried out approximately 310 ns long equilibrium MD simulation without any constraints. The visualization of the simulation snapshots (Supplementary Fig. 22c) and trajectory of the system suggests that the PAH[4] channels diffuse within the membrane and aggregate into larger clusters. The average root mean square deviation (RMSD) of the individual PAH[4] channel settles around 6 ± 1 Å. The available surface area per PAH[4] channel was 2.38 ± .08 nm^2 towards the end of the MD simulation (Supplementary Fig. 22d). As the simulation progressed, the water molecules permeated across the membrane through the PAH[4] channels. Supplementary Fig. 27 shows the pathways of water slipping across the membrane through a PAH[4] channel. We find that the average number of water molecules located within the central 1 nm-width region of the membrane is 51 ± 8, or approximately 2 water molecules per channel (Supplementary Fig. 22e). The average number of permeated water molecules per channel increases linearly with the simulation time (Supplementary Fig. 22f) and reaches 8 molecules per channel at the end of the 320 ns run.

To determine the effect of aggregation on the water permeability of the channels, we combined two units of PAH[4] channels to create a PAH[4] dimer (Supplementary Fig. 19 and 20a) in three different conformations (lateral, orthogonal, and inverted) as described above. Additionally, we also built one more system where the channels of the inverted conformation were filled with water at the beginning of the simulation. Following the similar simulation protocol used for the monomer array system, we simulated an array of 25 dimers of each conformation for 300 - 400 ns. The simulation snapshots of the system (Supplementary Fig. 23a-c) show that the PAH[4] dimers tend to assemble in to bigger clusters. Average RMSD of the individual dimer with respect to its initial structure converges to 6 ±1 Å. Average area per dimer reaches approximately 4.3 ± 0.1 nm^2 for all the conformations (Supplementary Fig. 23d). The number of water molecules in the center region of the membrane increases to 6 - 8 water molecules per dimer depending on the conformation. In the system that was filled with water at the beginning of the simulation, the number of water molecules decreases and reaches 6 - 8 at the end of the simulation (Supplementary Fig. 23e) The total number of water molecules permeated across the membrane ranges between 12 and 15 per dimer at the end of the simulations. Despite having the least number of water molecules in the channels, as compared to other configuration, the simulations shows that the PAH[4] orthogonal dimer is the most conductive. Transmembrane water permeation through the dimer happens via a continuous water wire guided by the triPhe side chains of PAH[4] (Supplementary Fig. 27), which is not seen in the monomer structure.

Monomer and dimer array simulations suggest that the aggregation of PAH[4] can produce water wires that span across the membrane region. The transmembrane water permeation also depends on the conformation of the PAH[4]. The histogram of the channel-wise permeated water molecules shows a wide range of the distribution in both monomer and dimers (Supplementary Fig. 24). Encouraged by these results, we created three all-atom clusters each containing eleven pre-aggregated dimeric unit of PAH[4], as described in the previous section. These lateral, orthogonal, and inverted cluster structures

were embedded in the POPC lipid bilayer membrane. All atom MD simulation of these structures reveal increased water permeability per PAH[4] molecule. Supplementary Fig. 24a-c and Supplementary Video 2 shows the simulation snapshots and trajectory, respectively, of the orthogonal cluster. Average surface area available per PAH[4] molecule from the last 200 ns equilibrium MD simulations is 2.06 ± 0.8 nm^2, 1.78 ± 0.7 nm^2, 2.24 ± 0.8 nm^2 for lateral, orthogonal and inverted clusters, respectively. The average number of water molecules in the central membrane region remain approximately 130 ± 10, 113 ± 10 and 128 ± 13 for lateral, orthogonal and inverted cluster structures, respectively. The number of water molecules that permeated across the membrane reached approximately 39 molecules per PAH[4] channel at the end of the 400 ns MD run of the lateral cluster structure, which we found to be the most conductive conformation. We observed water permeating across the membrane via several dynamic water-wire networks (Supplementary Fig. 21,25,27 and Supplementary Video 4 and 5).

Plotting the total number of permeated water molecules as a function of the simulation time, we computed the average single PAH[4] channel water permeability to increase from 0.022 to 0.092 molecules per ns from monomer/dimer to cluster structures, (Supplementary Fig. 21). Analysis of the MD simulation trajectories suggest that the slip and slide mechanism of water permeation observed in PAH[4] monomer and dimer array systems leads to continuous water wire networks in the PAH[4] cluster structures. These water channels are fundamentally different from the previously characterized transmembrane water channels. We did not observe any ions translocation across the membrane in our equilibrium MD simulation of PAH[4] channels in the monomer, dimer and cluster conformations. To probe the ion rejection efficiency of PAH[4] channel, we applied ± 1 V transmembrane bias in most conductive bouquet structure. Staring with snapshot of the system at the end of 400 ns free equilibration, we carried out additional 100 ns MD simulation with ± 1 V applied bias. Neither Na^+ nor Cl^- ion translocated through any of these channels in the applied bias simulation (Supplementary Video 3). Overall, all-atom MD simulation suggests that the aggregation of PAH[4] give rise to enhanced transmembrane water permeability via water-wire networks and that these channels do not facilitate ion transport.

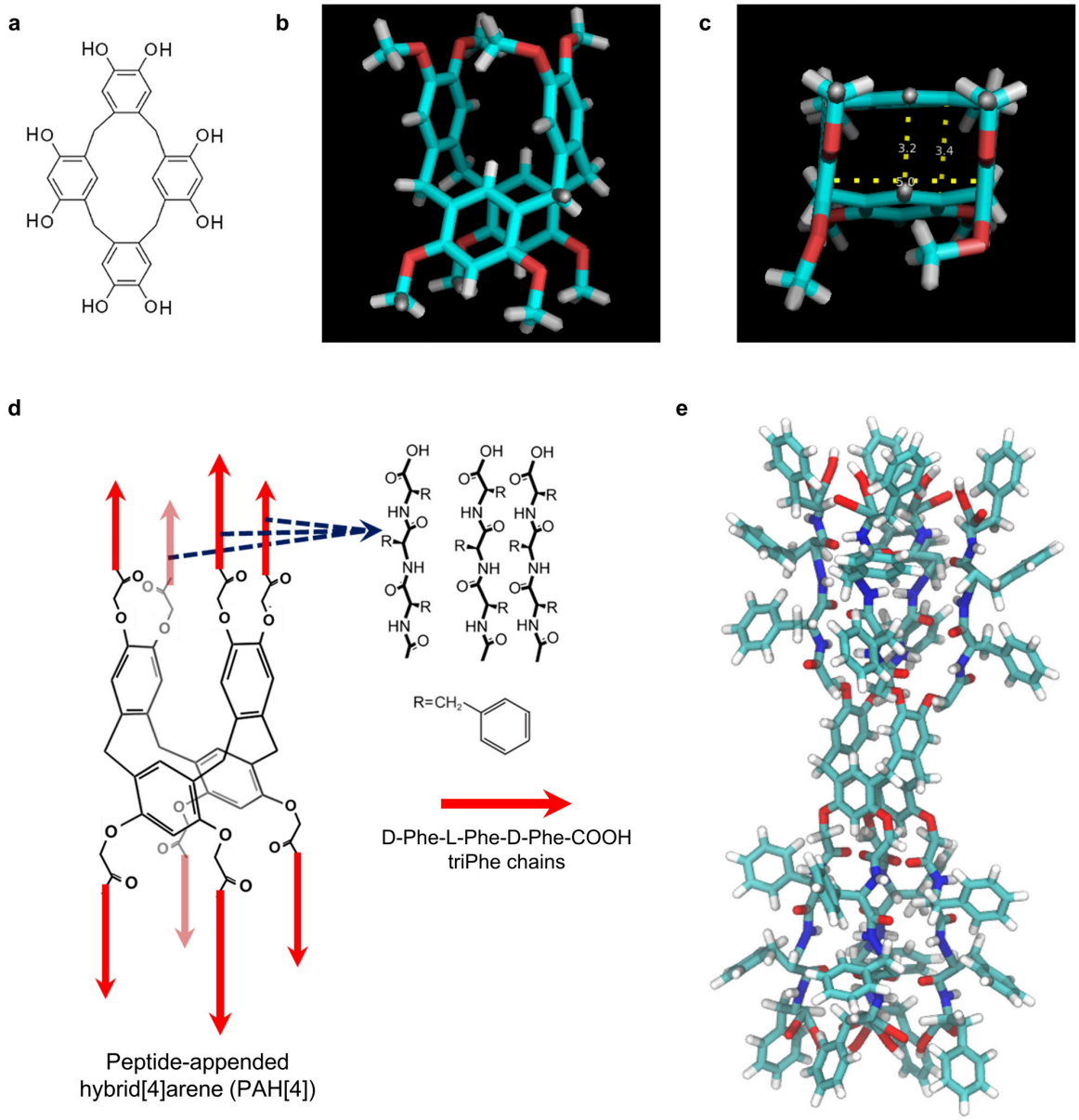

Supplementary Fig. 1. Molecular structure details of PAH[4] channel. **a**, Chemical structure of hybrid[4]arene macrocycle molecule. **b**, Crystal structure of hybrid[4]arene with methyl group substitution on hydroxide groups of hybrid[4]arenes[1]. **c**, Top-view of crystal structure of methyl-group substituted hybrid[4]arene, showing rectangular shaped central cavity with dimensions of ~3 Å × ~5 Å. **d**, Schematic illustration of molecular construction strategy of PAH[4] channel. Red arrows indicate directions of extended triPhe chains on hybrid[4]arene building template. **e**, Molecular modeling of prepared hybrid[4]arene channel.

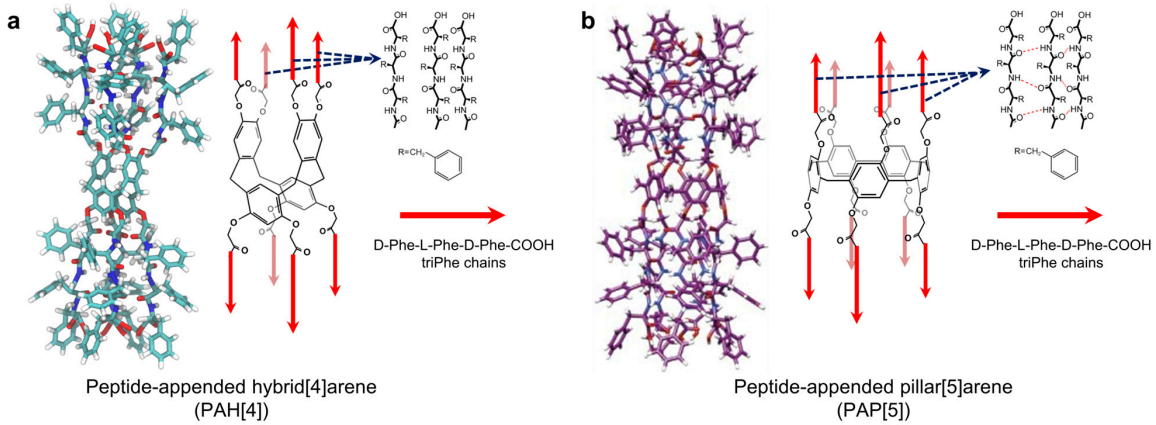

Supplementary Fig. 2. Structural comparison between PAH[4] and PAP[5] unimolecular artificial water channels. **a**,**b**, These two channels, PAH[4] (**a**) and PAP[5] (**b**), are structurally analogous except for that two different macromolecules, hybrid[4]arene and pillar[5]arene, are used as building templates for each channel, respectively. Pillar[5]arene has circular-shaped internal cavity (pore) with ~5 Å diameter which allowed both water and salt permeation[3]. Panel **b** figures are reproduced from the reference[3].

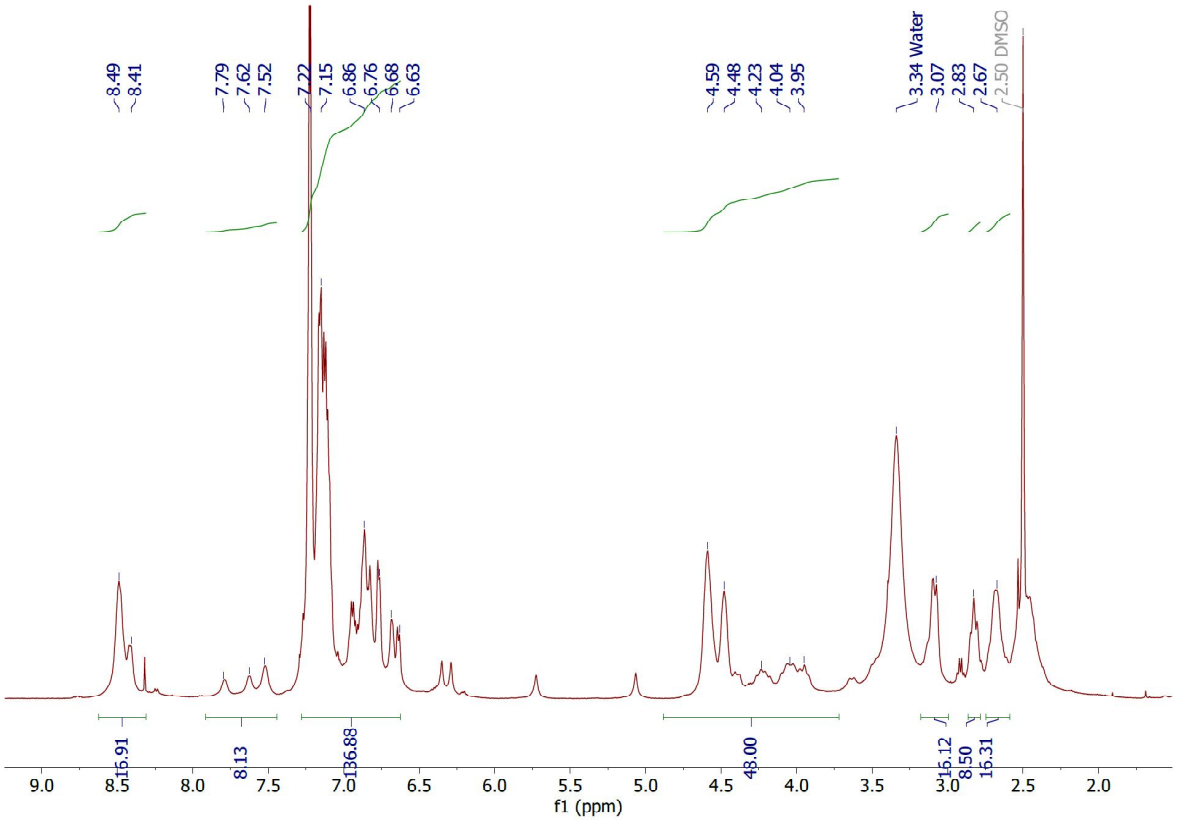

Supplementary Fig. 3. ^{1}H-NMR (DMSO-d_6) peaks of PAH[4]: δ 8.49-8.41 (m, 16 H), 7.79-7.52 (m, 8 H), 7.22-6.63 (m, 144 H), 4.59-3.95 (m, 48 H), 3.07 (m, 16 H), 2.83 (m, 8 H), 2.67 (m, 16 H).

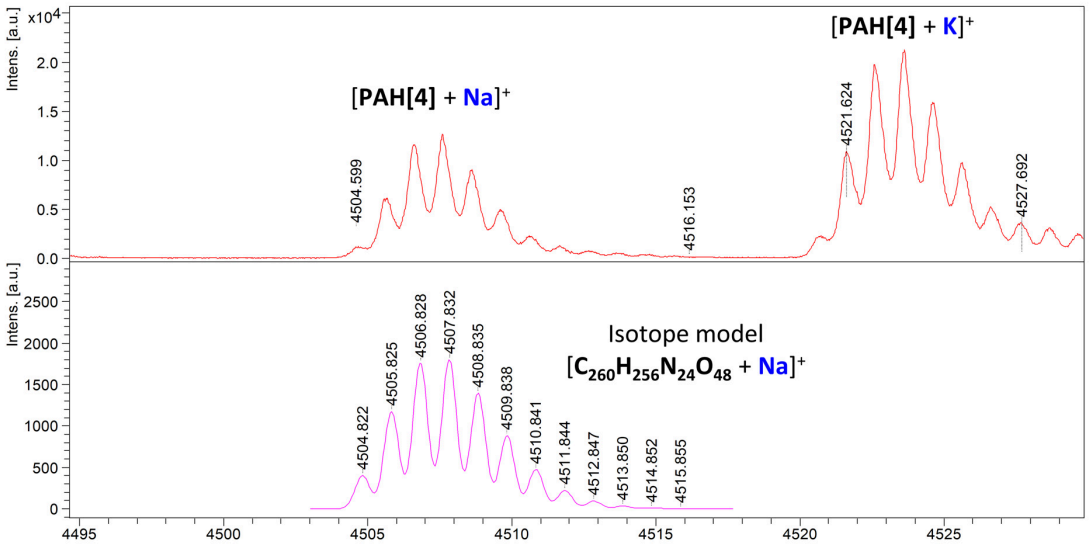

Supplementary Fig. 4. ICP-MS spectrum of PAH[4] channels (upper panel). Lower panel is a spectrum of PAH[4] isotope model ($C_{260}H_{256}N_{24}O_{48}$) of which peaks correspond with peaks of PAH[4] spectrum.

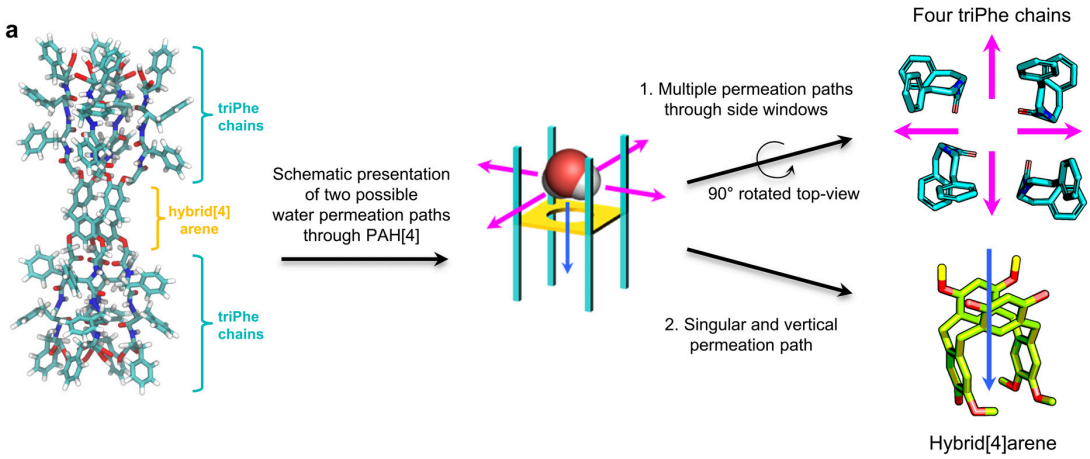

b

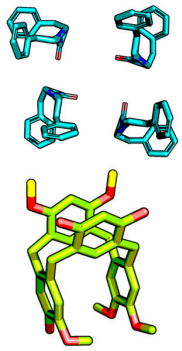

Region	Smiles ID	$\log P_{oct/wat}$
triPhe	O=C(CCc1ccccc1)N2#CC2Cc3ccccc3	3.85

Region	Smiles ID	$\log P_{oct/wat}$
Hybrid[4] arene	COc1c(O)cc2Cc3cc(c(OCC=O)cc3OCC=O)Cc4cc(c(OC)cc4Cc5cc(c(OCC=O)cc5OCC=O)Cc2c1)OC	4.99

Supplementary Fig. 5. Evaluation of energetically favorable water permeation paths through the PAH[4] channel. **a**, Schematic presentations of two possible water permeation paths through PAH[4] channels; one is permeating through triPhe chains (magenta arrows) and the other is permeating vertically through hybrid[4]arene (blue arrow). **b**, Hydrophobicity of each triPhe chains and hybrid[4]arene was evaluated using $\log P_{oct/wat}$ value; $P_{oct/wat}$ is the partition coefficient between octane and water. Lower $\log P_{oct/wat}$ value of triPhe chains indicates that triPhe chains are relatively hydrophilic compared to the hybrid[4]arene central ring. This implies that water molecules sitting inside the channel would be more favorable to pass through triPhe chains rather than hybrid[4]arene if such a path was feasible.

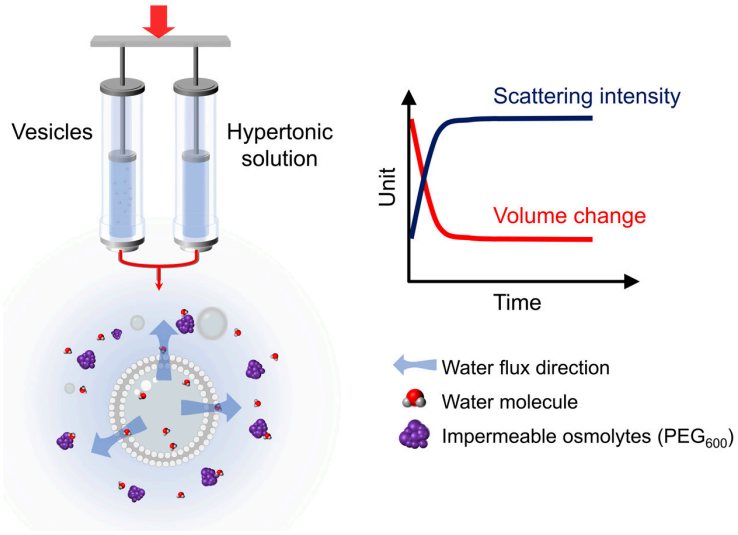

Supplementary Fig. 6. Schematic illustration of basic principle of measuring water permeability of vesicular membranes using stopped-flow instrument. Water efflux driven by osmotic pressure induces shrinkage of vesicles and this kinetic information is related with membranes' permeability as described in supplementary text. The seemingly inversed trends between size change of vesicles and scattering intensity is attributed to destructive interferences of light scattering caused by several factors such as detection angle (90º) and comparable vesicle size (~200 nm) to the wavelength (600 nm) of incident light (e.g., vesicle sizes > 1/10 of the wavelength) [27]. The permeability measurements under swelling mode were performed by placing the osmolytes inside of the vesicles and imposing inwardly driven osmotic pressure.

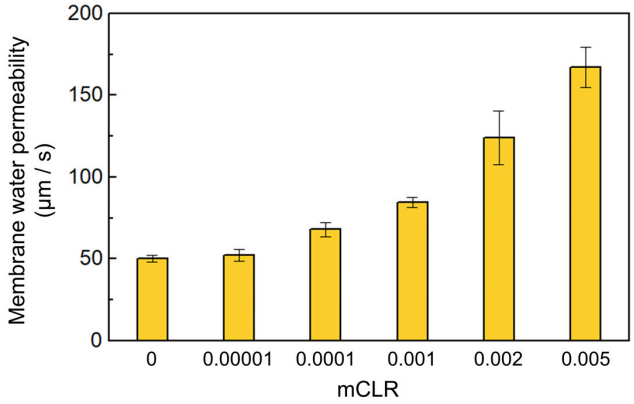

Supplementary Fig. 7. Water permeabilities of PC/PS lipid vesicular membranes with different amounts (molar ratio of channels to lipids, mCLR) of reconstituted PAH[4] channels. mCLR 0 indicates control PC/PS lipid membranes. For the permeabilities calculated based on equation (9), PAH[4]-mediated membrane water permeabilities were calculated as 0.081 ± 0.003, 24 ± 3.0, 84 ± 9.0, 132 ± 10.3, and 150 ± 6.7 μm/s for mCLRs of 0.00001, 0.0001, 0.001, 0.002, and 0.005 respectively, by subtracting background (control) permeability from presented values in this figure.

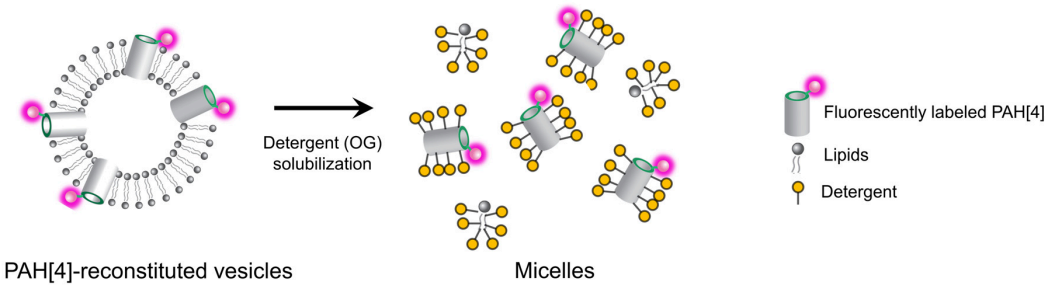

Supplementary Fig. 8. Schematic illustration of counting channel numbers per vesicles using FCS technique. Using FCS, the number of "fluorescent particles" in the system could be counted from the autocorrelation function. These numbers correspond with the number of reconstituted vesicles (N_{chan}) and the number of PAH[4] channels (N_{chan}), before and after detergent solubilization, respectively.

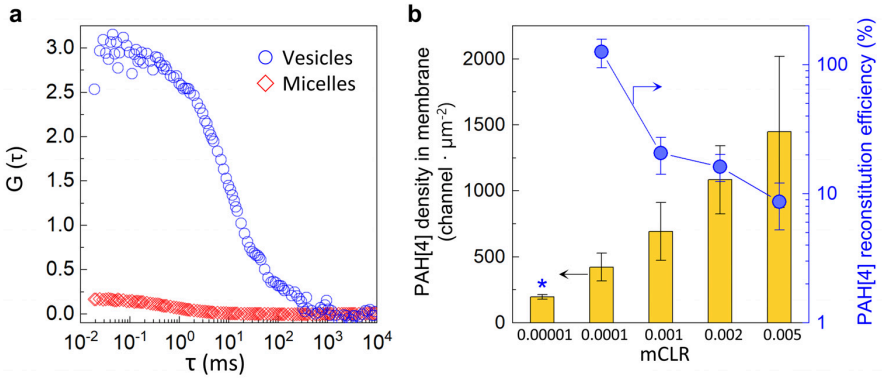

Supplementary Fig. 9. FCS analyses for obtaining PAH[4] channel insertion efficiency (channel density) in lipid membranes. **a**, Representative autocorrelation functions, G(τ), of PAH[4]-reconstituted vesicles (mCLR 0.005) and labeled PAH[4] micelles, before (blue circles) and after (red diamonds) detergent solubilization with 2.5% OG, respectively. **b**, PAH[4] channel densities in reconstituted lipid membranes (channel numbers per μm^2 membrane area) at different mCLRs. These values were used to calculate single channel water and ion permeabilities. Theoretical PAH[4] channel reconstitution efficiency was calculated and presented with blue circles. The cross sectional area of single lipid molecules was estimated as ~60 $Å^2$. *The very low number of inserted channels lead to inconsistent measurements over several cycles which we deem unreliable and are hence not shown here. This might be attributed to challenges with maintaining consistency in the lipid vesicle preparation and channel insertion process (particularly the difficulty of accounting for loss of lipid during self-assembly and extrusion steps) at low channel concentrations.

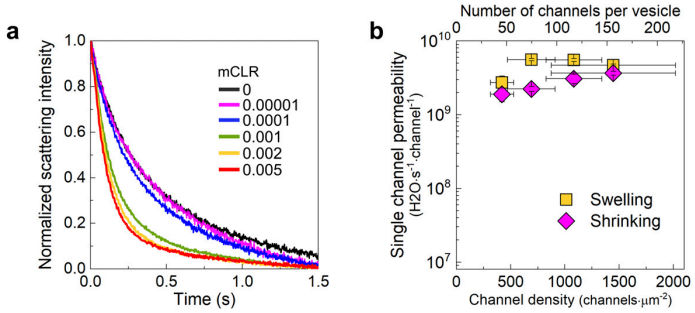

Supplementary Fig. 10. PAH[4]-reconstituted vesicular membrane permeability measurements under swelling and shrinking modes indicate a small (1.3 - 2.5 fold) difference in the single channel permeability. **a**, Representative light scattering traces of vesicles at different mCLRs measured in a shrinkage mode. **b**, Calculated single PAH[4] channel permeability measured in both swelling and shrinking modes.

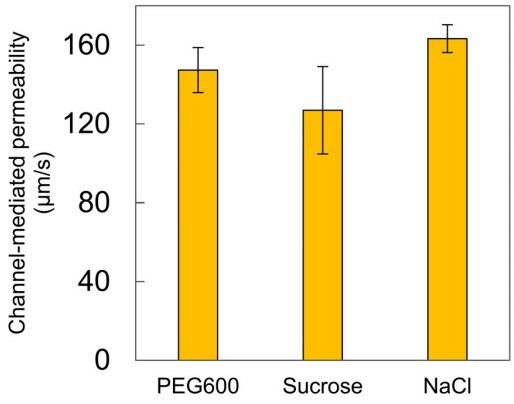

Supplementary Fig. 11. PAH[4]-reconstituted membranes' (mCLR 0.005) PAH[4] channel mediated permeability measured using different types of osmolytes. It has been reported that chaotropic osmolytes could enhance the water permeation rate through CNTPs via disrupting the H-bonds between water molecules. However, in case of PAH[4] channels, no permeability difference was observed regardless of the types of osmolytes used, including PEG600 (chaotrope), sucrose (kosmotrope), and NaCl (a slight kosmotrope).

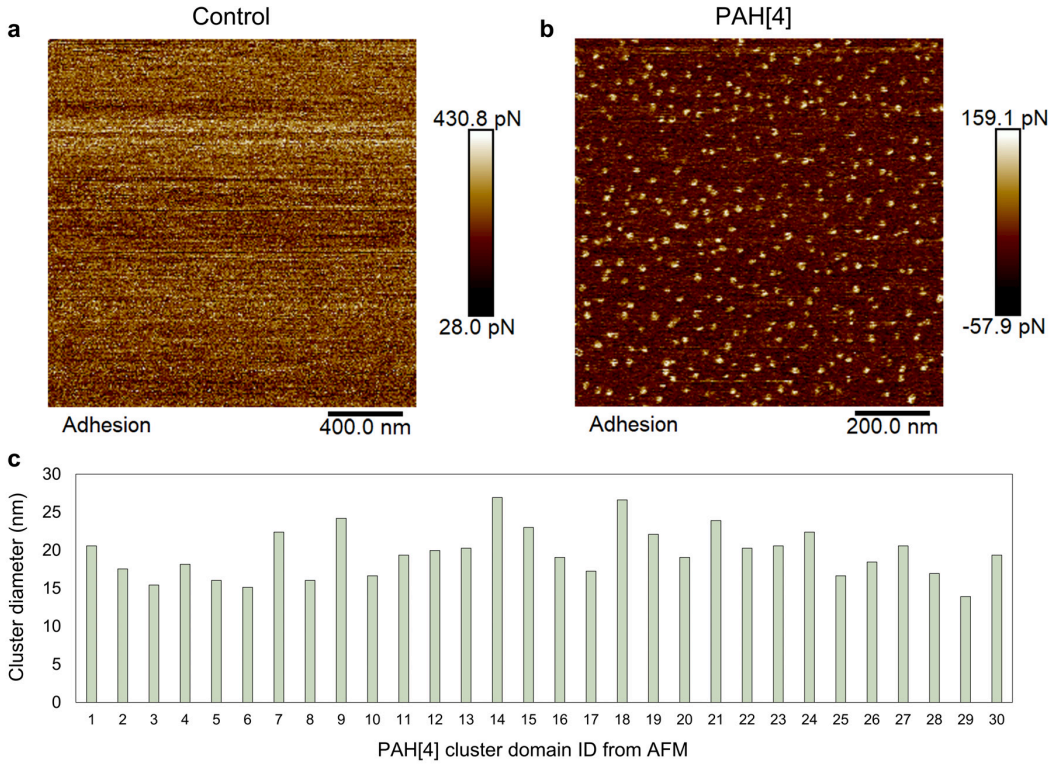

Supplementary Fig. 12. a,**b**, AFM images of control (**a**) and PAH[4] (**b**) -reconstituted supported lipid bilayer membranes on mica. **c**, Line-scan analyses of randomly chosen 30 PAH[4] clusters from AFM images. The average PAH[4] domain diameter was observed to be 19.6 ± 3.2 nm with an average cluster area of 301 ± 8 nm^2. Considering the cross-sectional area of each PAH[4] monomer to be about ~2 nm^2 (from MD simulations), each cluster domain consists of 150 ± 4 PAH[4] monomers. The supported bilayer sample for AFM experiments were prepared using mCLR 0.005 PAH[4]-reconstituted vesicles and the number of PAH[4] channels per mCLR 0.005 vesicle was measured to be 110 ± 31 from FCS experiments, indicating that the cluster size from AFM experiments (150 ± 4 PAH[4] channels) translates well into the number of PAH[4] subunits per vesicle (110 ± 31 PAH[4] channels) estimated by FCS.

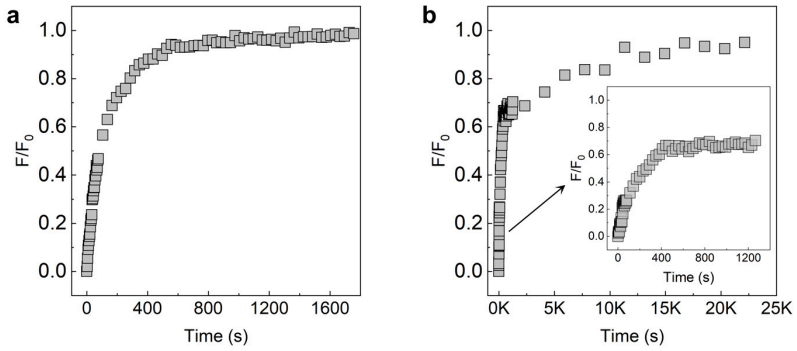

Supplementary Fig. 13. a,**b**, Representative FRAP curves for TR-DHPE lipids (**a**) and labeled-PAH[4] (**b**) embedded planar PC/PS lipid membranes.

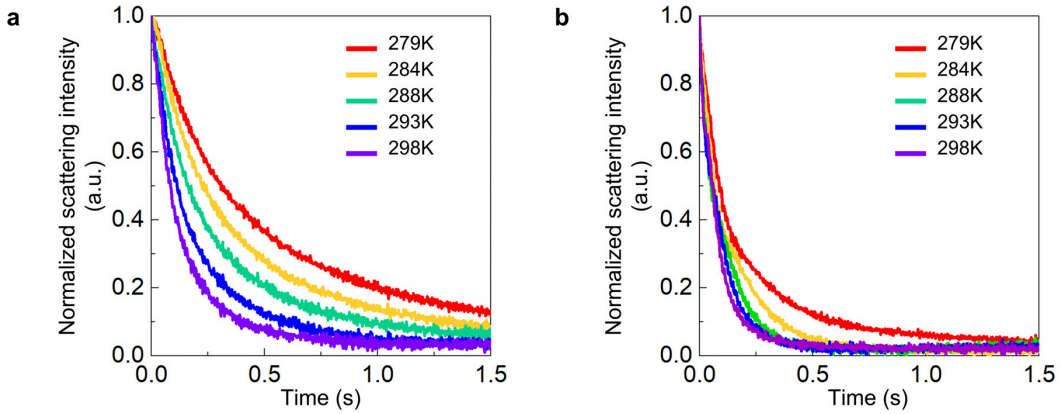

Supplementary Fig. 14. a,**b**, Stopped-flow scattering traces of bare lipid vesicles (**a**) and PAH[4]-reconstituted vesicles (mCLR 0.002) (**b**) at different temperatures (K) to calculate the activation energy of water permeation.

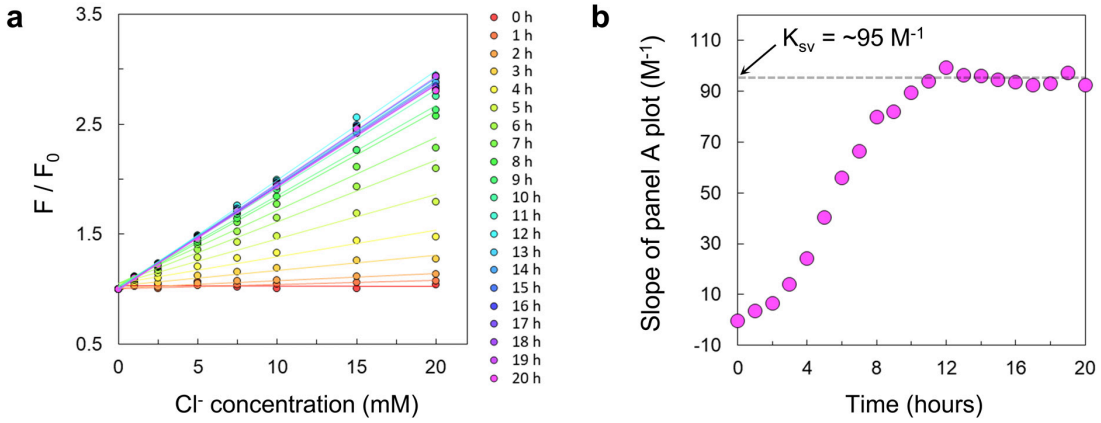

Supplementary Fig. 15. Determination of K_{sv} constant of lucigenin dyes inside lipid vesicles of ~200 nm diameter. **a**, Plotting of F/F_0 as a function of Cl^- concentration (mM) with monitoring time (hours). **b**, Slope change of panel **a** plots as a function of monitoring time. Slopes became consistent after 10 hours of exposing vesicles to different Cl^- concentration environments, indicating that, after 10 hours, intravesicular Cl^- concentrations were equilibrated with extravesicular environments. K_{sv} constant is determined as ~95 M^{-1}.

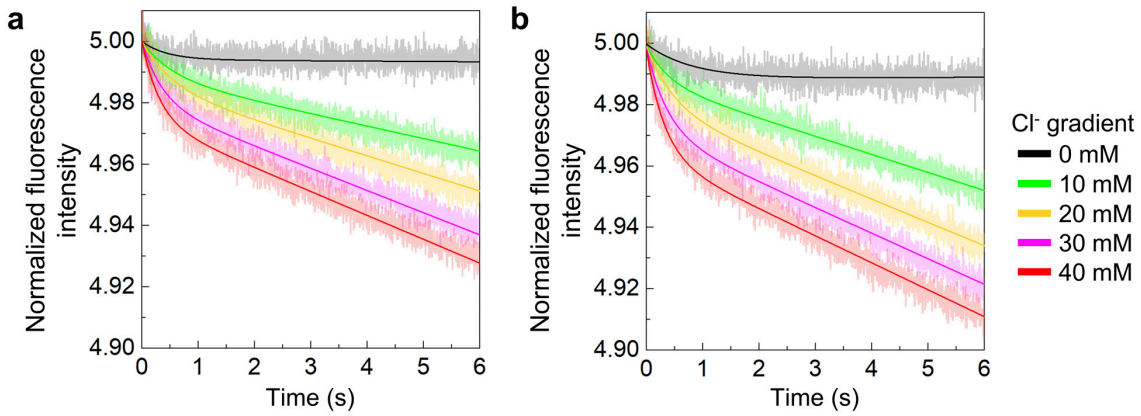

Supplementary Fig. 16. a,**b**, Representative fluorescence traces of control PC/PS vesicles (**a**) and PAH[4]-reconstituted vesicles (mCLR 0.005) (**b**) for Cl^- permeability test with lucigenin dyes. Translucent backgrounds are raw signals obtained from stopped-flow experiments and solid lines are fitted equations. Slightly enhanced Cl^- permeability (rapid quenching of fluorescence intensity due to fast Cl^- influx into vesicles) of PAH[4]-vesicles can be seen when traces are compared between control and channel vesicles.

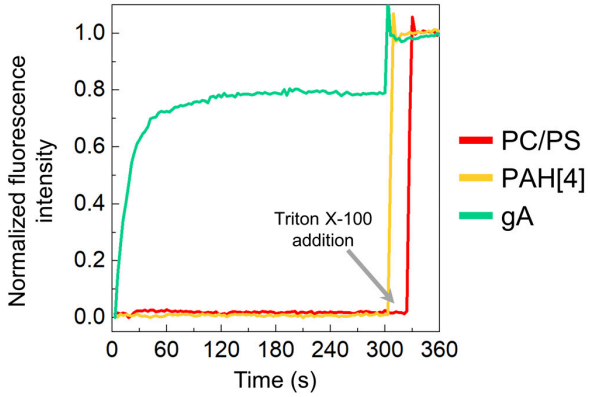

Supplementary Fig. 17. Representative traces of fluorescence intensity changes of HPTS dyes encapsulated in lipid vesicles, after vesicles were exposed to lower proton concentration environment (higher pH). No significant fluorescence intensity change is shown for both control (PC/PS) and PAH[4]-reconstituted (mCLR 0.005) vesicles, indicating that PAH[4]-vesicular membranes can reject Na^+ ions as efficiently as control lipid membranes. As a positive control, gA, which is well known as a cation transporting peptide, was tested as a positive control. Vesicles with gA showed fast increase fluorescence intensity. This is attributed to that Na^+ permeation through vesicular membranes that mitigates cationic electrostatic imbalance between inside and outside of vesicles and allow faster diffusion of H^+ from inside to outside of vesicles, resulting in enhanced fluorescence intensity of H^+-sensitive HPTS dyes.

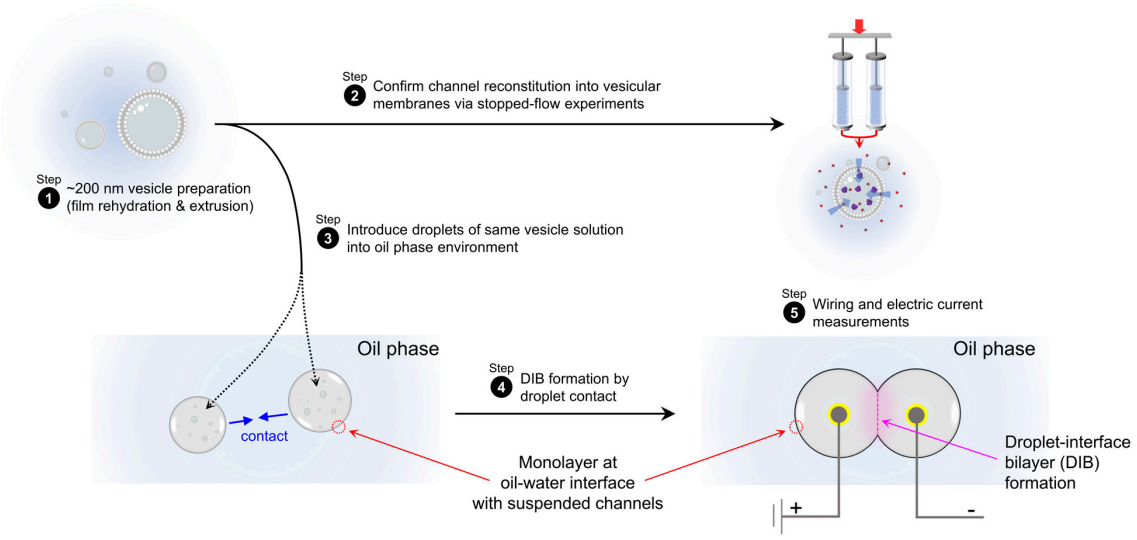

Supplementary Fig. 18. Work-flow of DIB based electrical current measurements across channel-embedded lipid bilayer membranes. The vesicles were first prepared by conventional film rehydration and extrusion processes, in which channel insertion was verified by stopped-flow experiments. After that, the same vesicles were introduced into DIB set-up to form the micron-scale bilayer membranes in between two droplets. Since the PAH[4] channel reconstitution density in mCLR 0.005 vesicles (which was used to form DIB bilayer) was ~1,500 channels per μm^2, ~1.1×10^8 PAH[4] channels would possibly be present across the DIB interface (circular area with ~300 µm in diameter), showing that the large DIB bilayer area maximizes the chance of channel incorporation, while the possibility that the channels escaped from the membrane (oil-water interface) into oil-phase still exist between the step 3 and 4. Therefore, structurally analogous PAP[5] channels were also tested as positive control to show that triPhe-chain appended unimolecular AWC structures could be successfully held up inside the membrane during DIB formation. Also, as comparison of DIB technique to conventional planar lipid bilayer based electrical current measurements, the amount of oil retained in a DIB is identical to that of a planar bilayer membrane formed across the aperture of a substrate using the lipid painting technique. Further, many bilayers have been formed across apertures painted with lipids dissolved in decane or pentane, smaller oil molecules that would result in higher amounts of oil in the bilayer compared to hexadecane. We used hexadecane to strategically minimize the amount of oil in the membrane and its potential effect on PAP[5] and PAH[4] channels.

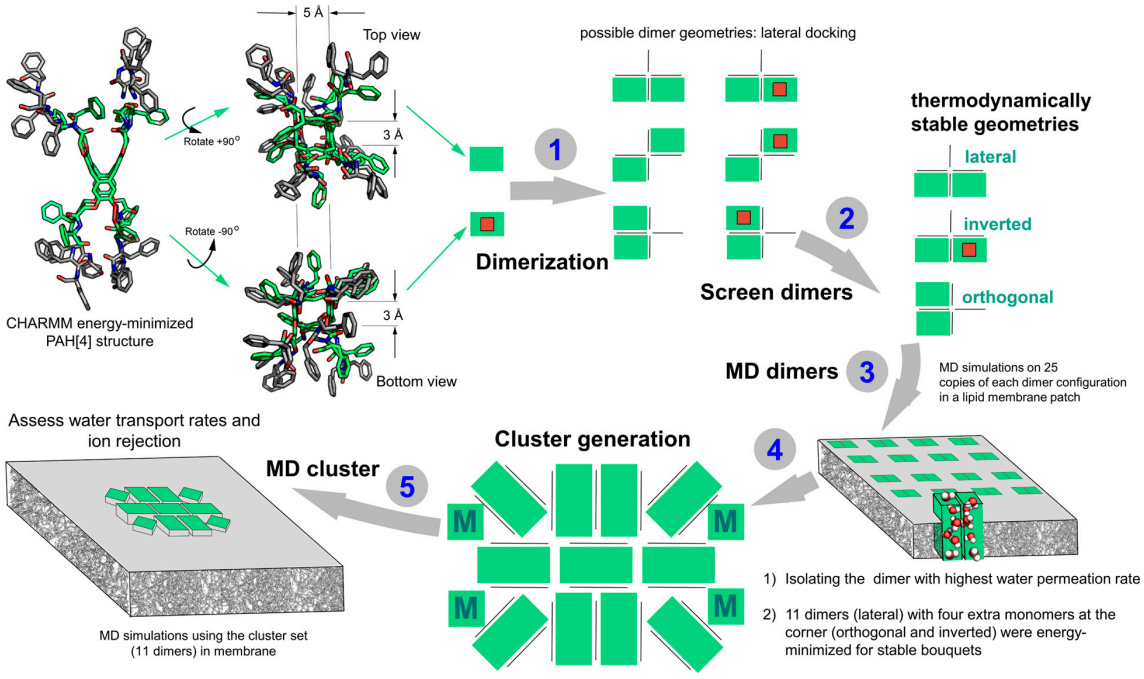

Supplementary Fig. 19. Overview of the *in silico* procedure for generating PAH[4] cluster configurations to model oligomeric PAH[4] cluster geometry in lipid bilayer membranes

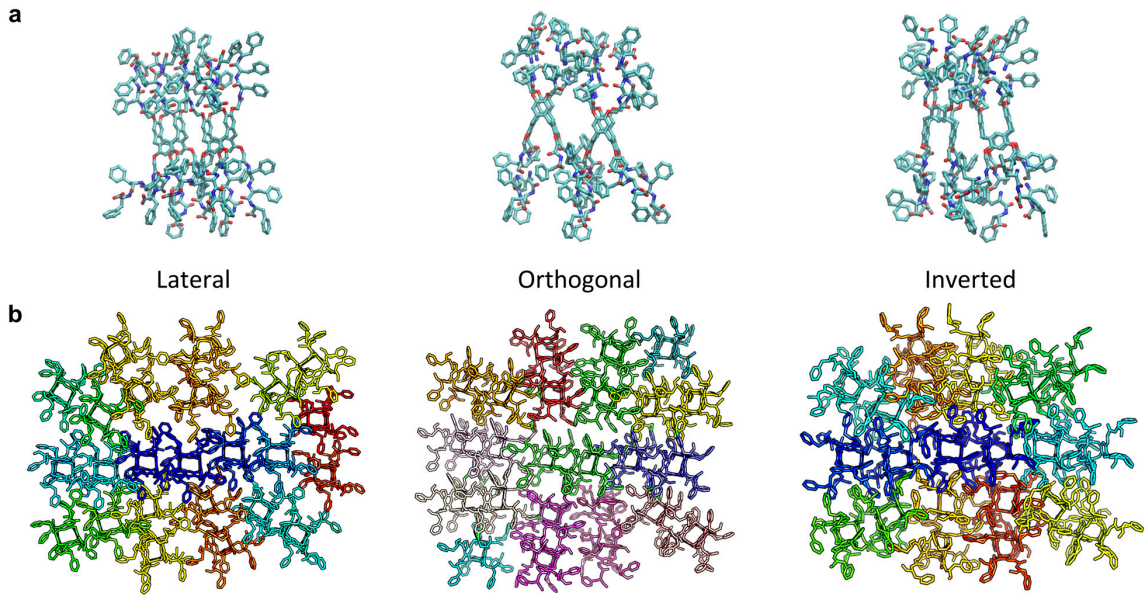

Supplementary Fig. 20. a,**b**, Three representative lateral, orthogonal, and inverted molecular configurations of dimeric (side-view) (**a**) and cluster (top-view) (**b**) PAH[4]s generated *in silico*.

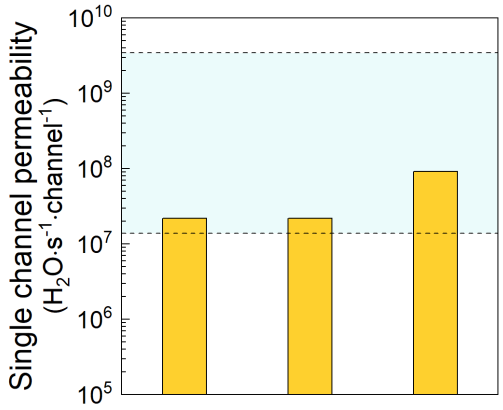

Supplementary Fig. 21. Average water permeability per PAH[4] channel in MD simulation of a lipid bilayer membrane containing an array of PAH[4] monomers and most conductive dimers and 22-mer clusters. Data were averaged over MD trajectories spanning ~400 ns. The shaded area represents the PAH[4] permeability range measured by experiments.

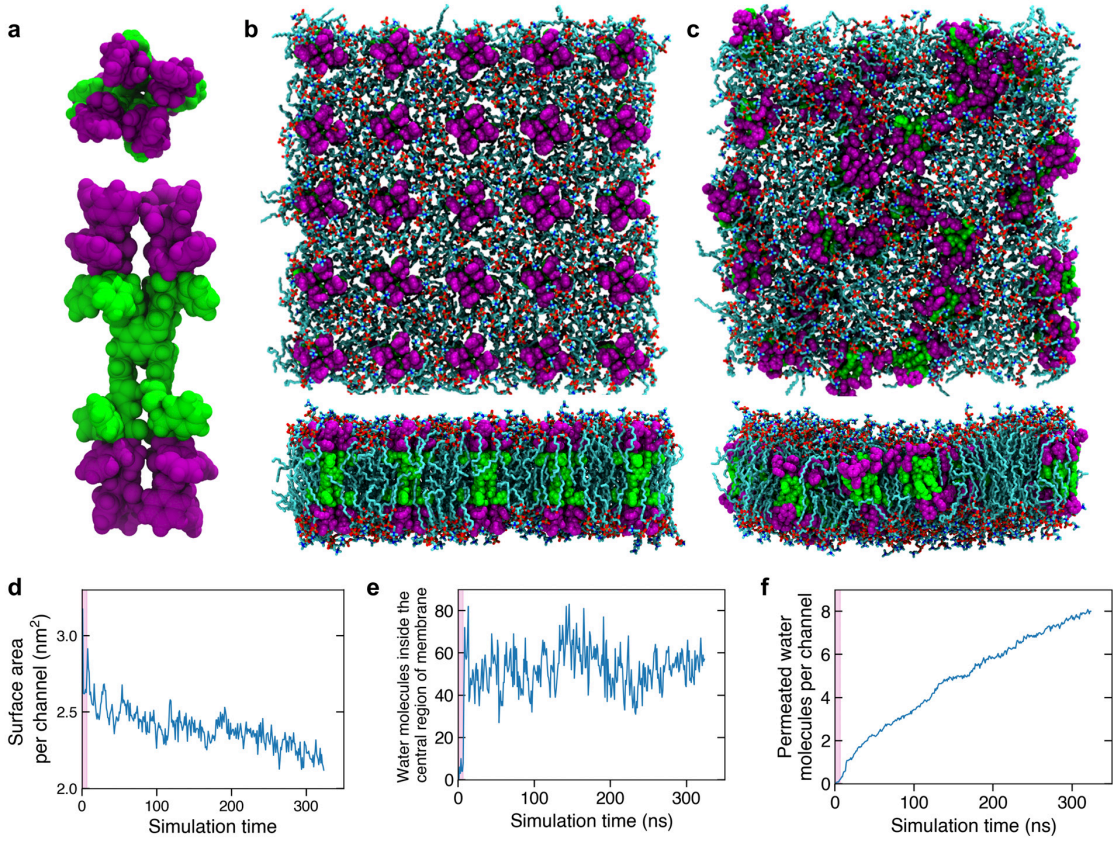

Supplementary Fig. 22. Explicit-solvent MD simulation of PAH[4] monomer array. **a**, The all-atom model of PAH[4] channel in van der Wall (vdW) representation. The hybrid[4]arene macromolecule and the nearest phenylalanine is shown in green and the remaining phenylalanine arms are shown in purple. **b**, Instantaneous snapshot of an array of 25 PAH[4] embedded in pre-equilibrated POPC lipid bilayer membrane (14.4 × 14.4) nm at beginning of the MD simulation. **c**, Snapshot of the system at the end of 320 ns of equilibrium MD simulation. In the panels of a - c, the top and bottom panel show the top and side view of the system respectively. Lipid molecules are shown as cyan molecular bonds. Water and ions are not shown for clarity. **d**, The average surface area occupied by a channel as a function of simulation time. **e**, The number of water molecules present in the central 1 nm wide region of the membrane as a function of simulation time. **f**, The cumulative number of permeated water molecules with respect to the simulation time. In panels d – f, the shaded region indicates the first 5 ns of the equilibration simulation performed having all non-hydrogen atoms of the PAH[4] molecules harmonically restrained to their initial coordinates.

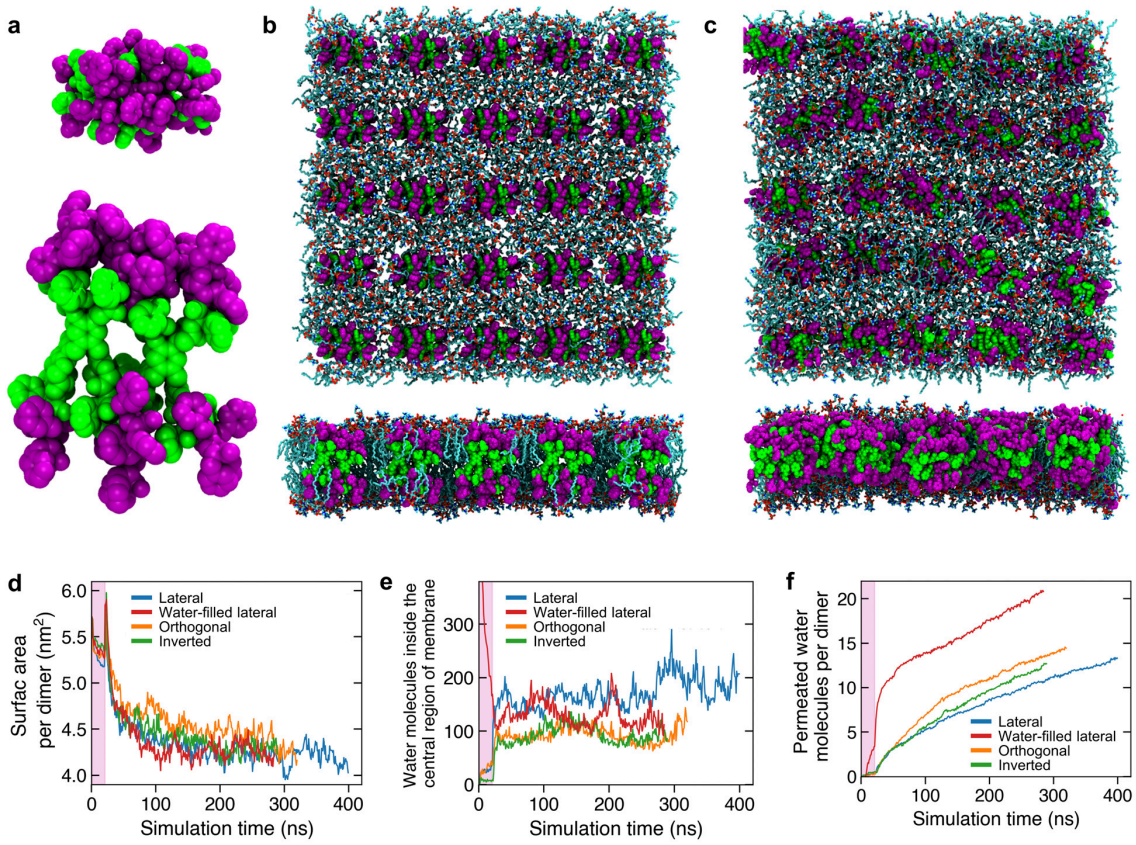

Supplementary Fig. 23. Explicit-solvent MD simulation of PAH[4] dimer arrays. **a**, The all-atom model of orthogonal PAH[4] dimer in vdW representation. **b**, A snapshot of 25 PAH[4] dimers embedded into POPC lipid bilayer membrane at the beginning of the MD simulation. **c**, Representative snapshot of the system (orthogonal dimer) at the end of 300 ns of equilibrium MD simulation. In the panels of a - c, the top and bottom panel show the top and side view of the system respectively. Water and ions are not shown for clarity. **d**, The average surface area occupied by a dimer as a function of simulation time. **e**, The number of water molecules present in the central 1 nm wide region of the membrane as a function of simulation time. **f**, The cumulative number of permeated water molecules with respect to the simulation time. In panels d - f, the shaded region indicates the first 20 ns of the equilibration simulation performed having all non-hydrogen atoms of the PAH[4] molecules harmonically restrained to their initial coordinates.

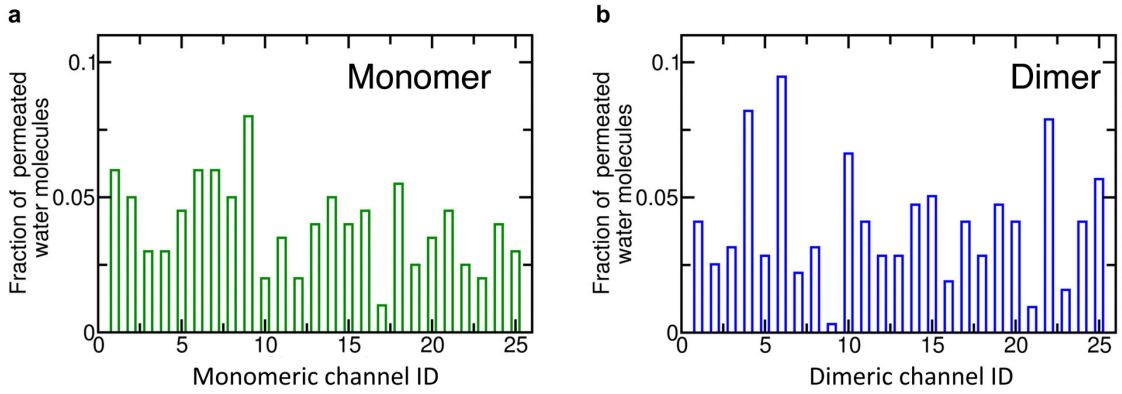

Supplementary Fig. 24. Contribution of individual channels or dimers to total simulated water conductance. **a**,**b**, The histograms show the fraction of water molecules permeated through individual PAH[4] channels (**a**) or dimers (**b**); the dimers had orthogonal conformation.

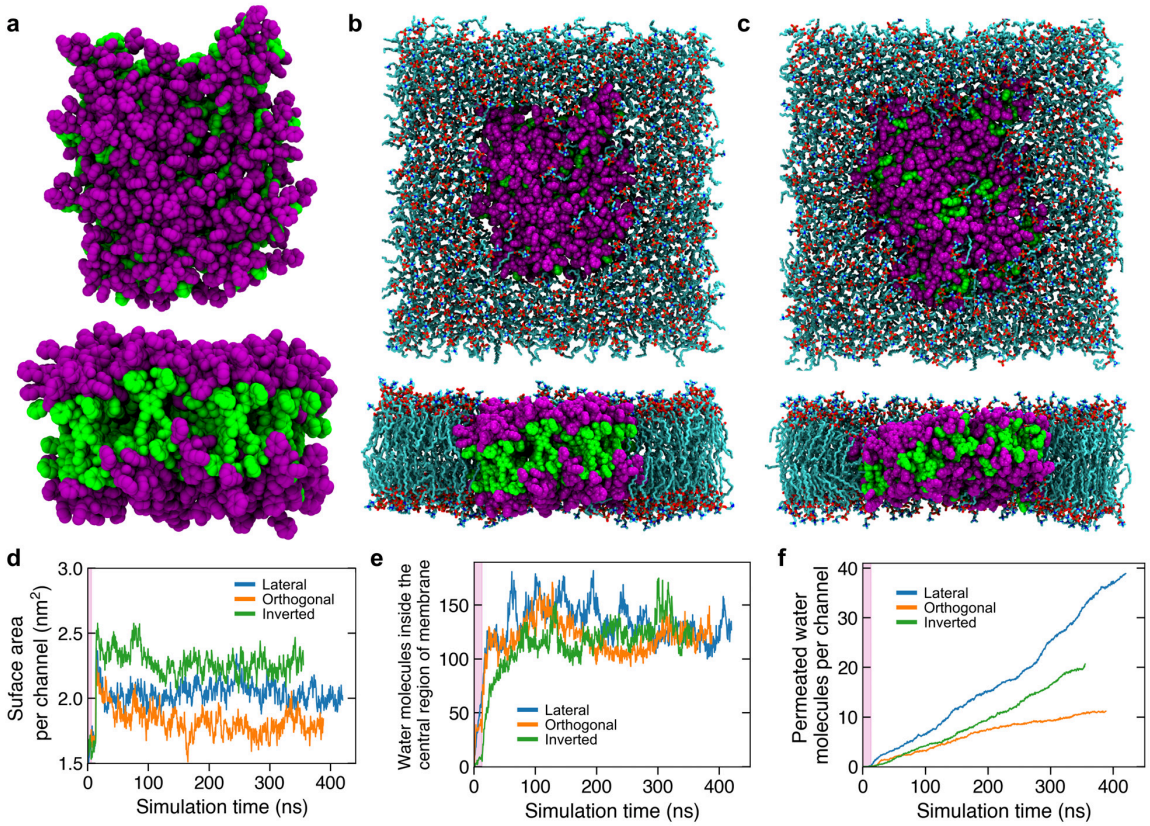

Supplementary Fig. 25. Explicit-solvent MD simulation of pre-assembled PAH[4] clusters in a lipid bilayer membrane. **a**, The all-atom model of pre-assembled PAH[4] cluster forming a "bouquet" like structure. **b**, A snapshot of lateral PAH[4] clusters embedded into a pre-equilibrated POPC lipid bilayer membrane at the beginning of the MD simulation. **c**, Representative snapshot of the system (lateral cluster) at the end of 400 ns of equilibrium MD simulation. In the panels of a - c, the top and bottom panel show the top and side view of the system respectively. Water and ions are not shown for clarity. **d**, The average surface area occupied by a PAH[4] channel in a cluster as a function of simulation time. **e**, The number of water molecules present in the central 1 nm wide region of the membrane with respect to the simulations time. **f**, The cumulative number of permeated water molecules increases with respect to the simulation time. In panels d - f, the shaded region indicates the first 12 ns of the equilibration simulation performed having all non-hydrogen atoms of the PAH[4] molecules harmonically restrained to their initial coordinates.

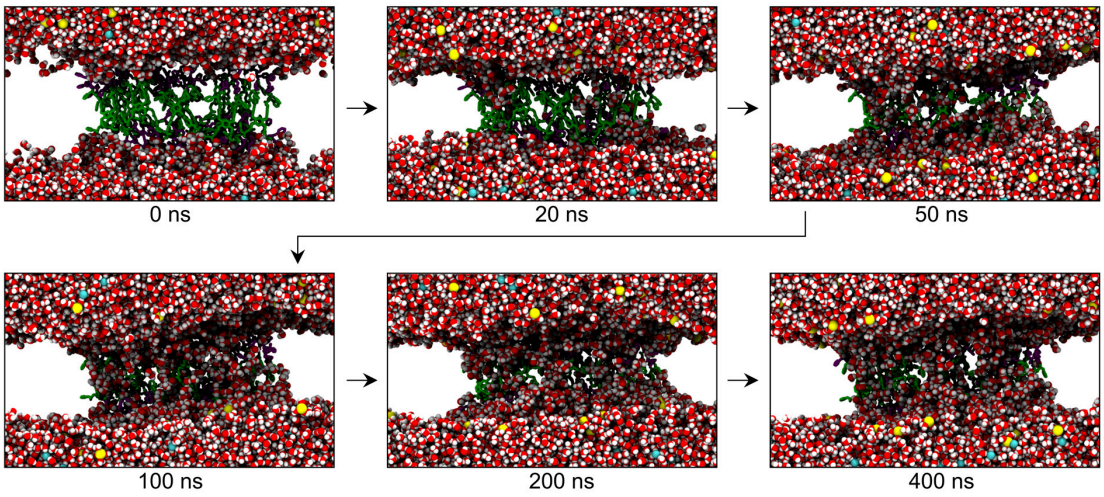

Supplementary Fig. 26. Snapshots of PAH[4] 22-clusters highlights the formation of the transmembrane water wires after 0, 20, 50, 200, and 400 ns of equilibrium MD simulation. Water and ions are shown using red (oxygen), white (hydrogen), yellow (sodium) and cyan (chloride) vdW spheres. PAH[4] channels are shown using green/purple molecular bonds.

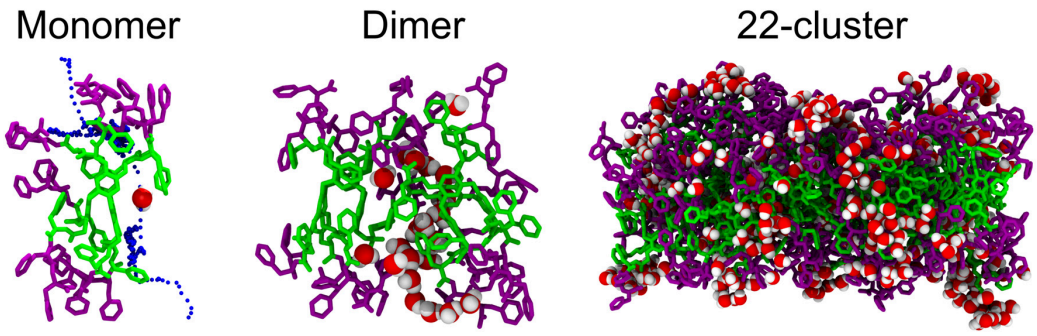

Supplementary Fig. 27. Instantaneous MD snapshots of representative monomer, dimer and cluster configurations showing water permeation. Blue points in monomer structure show the path of water slipping through triPhe side chains, which was not continuous.

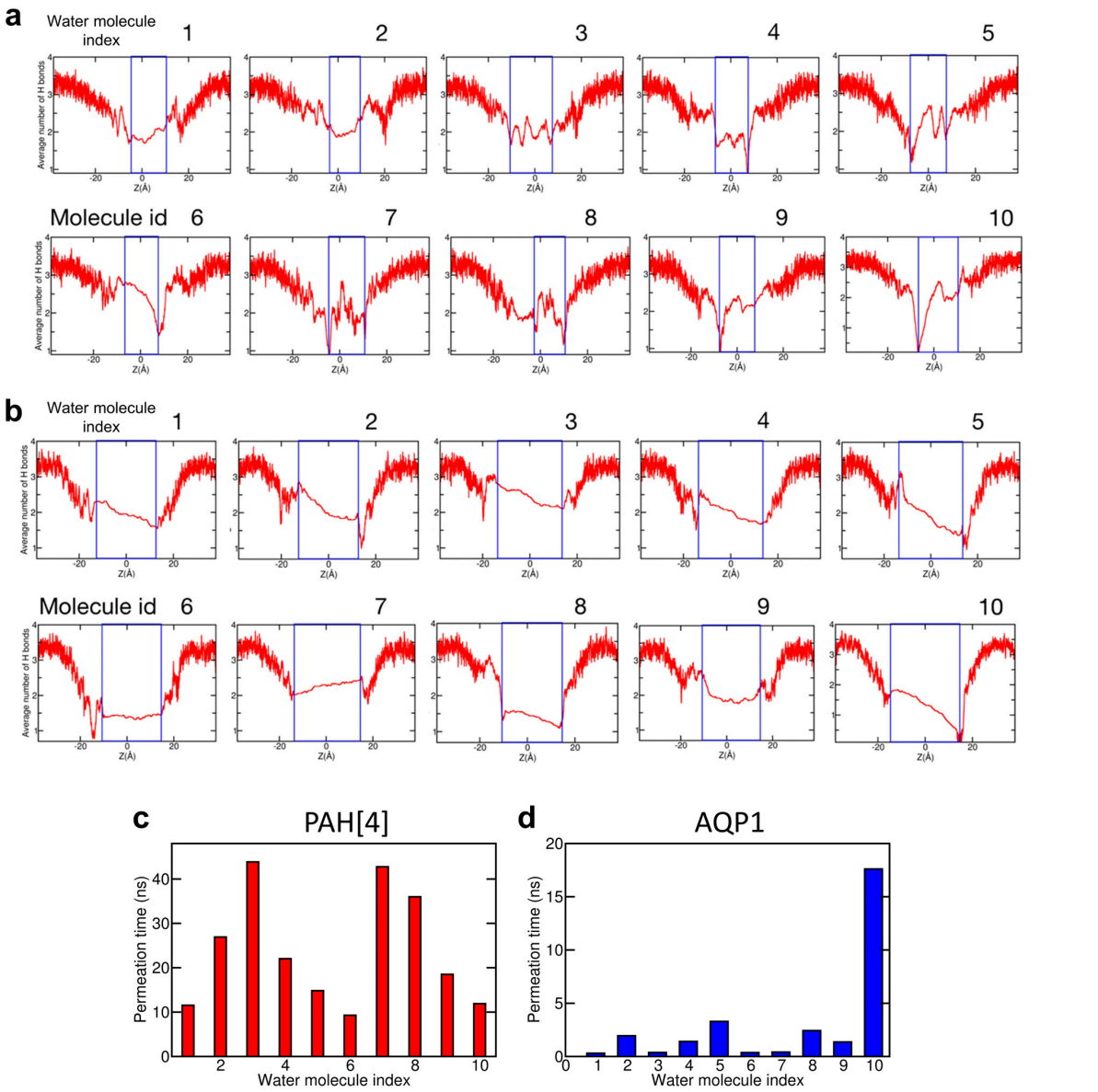

Supplementary Fig. 28. **a**,**b**, The number of H-bonds formed by ten water molecules as a function of their Z coordinate that permeated through a PAH[4] cluster (**a**) or AQP1 tetramer (**b**). These water molecules were chosen randomly from a set of ~800 and 400 water molecules permeated through PAH[4] and AQP1, respectively. The blue box specifies the constriction region used to perform the calculation of the permeation time and the permeation path length. **c**,**d**, Panels (**c**) and (**d**) specify the permeation time for each water molecules.

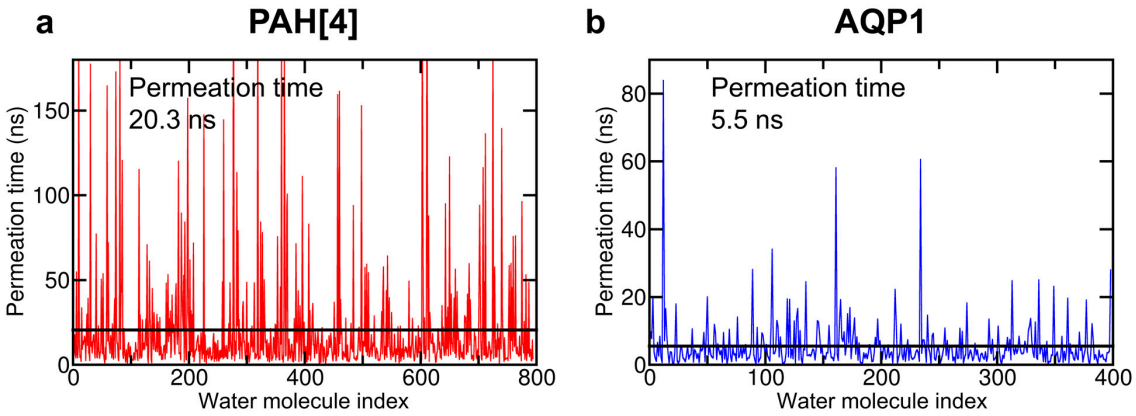

Supplementary Fig. 29. a,**b**, The time taken by each water molecule to pass through the constriction of the PAH[4] cluster (**a**) and of the AQP1 tetramer (**b**). The channel's constrictions were defined according to the average number of H-bonds plot (Fig. 4c) within 9 and 14 Å of the membrane's midplane for PAH[4] and AQP1, respectively.

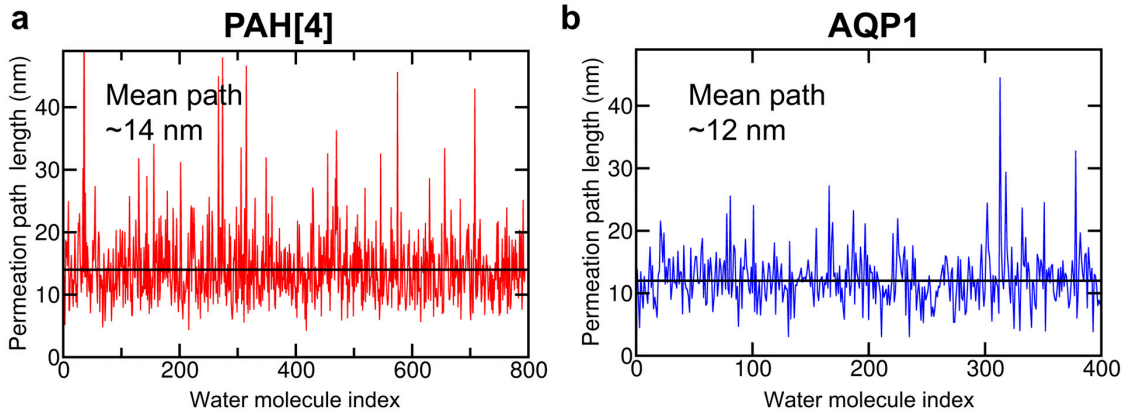

Supplementary Fig. 30. a,**b**, The length of the path travelled by each water molecule through the constriction of the PAH[4] (**a**) and AQP1 (**b**) channels. To compute the average distance travelled by a water molecule, we first determined the average X and Y coordinates of each water molecule along the Z axis in 1Å bins and summed up the distance between the average water coordinates in the nearest bins (18 bins for PAH[4] and 28 bins for AQP1).

References

1. Boinski, T., Cieszkowski, A., Rosa, B. & Szumna, A. Hybrid [n]Arenes through Thermodynamically Driven Macrocyclization Reactions. *J. Org. Chem.* **80**, 3488-3495 (2015).

2. Chen, L. et al. Chiral Selective Transmembrane Transport of Amino Acids through Artificial Channels. *J. Am. Chem. Soc.* **135**, 2152-2155 (2013).

3. Shen, Y.-x. et al. Highly permeable artificial water channels that can self-assemble into two-dimensional arrays. *Proc. Natl. Acad. Sci. USA* **112**, 9810-9815 (2015).

4. Shen, Y.-x. et al. Achieving high permeability and enhanced selectivity for Angstrom-scale separations using artificial water channel membranes. *Nat. Commun.* **9**, 2294 (2018).

5. De Cola, C. et al. Size-dependent cation transport by cyclic α-peptoid ion carriers. *Org. Biomol. Chem.* **7**, 2851-2854 (2009).

6. Lang, C. et al. Biomimetic Transmembrane Channels with High Stability and Transporting Efficiency from Helically Folded Macromolecules. *Angew. Chem. Int. Ed.* **55**, 9723-9727 (2016).

7. Ren, C. et al. Pore-Forming Monopeptides as Exceptionally Active Anion Channels. *J. Am. Chem. Soc.* **140**, 8817-8826 (2018).

8. Horner, A. et al. The mobility of single-file water molecules is governed by the number of H-bonds they may form with channel-lining residues. *Sci. Adv.* **1**, e1400083 (2015).

9. Hannesschläger, C., Barta, T., Siligan, C. & Horner, A. Quantification of Water Flux in Vesicular Systems. *Sci. Rep.* **8**, 8516 (2018).

10. Saffman, P. G. & Delbrück, M. Brownian motion in biological membranes. *Proc. Natl. Acad. Sci. USA* **72**, 3111-3113 (1975).

11. Petrov, E. P. & Schwille, P. Translational Diffusion in Lipid Membranes beyond the Saffman-Delbrück Approximation. *Biophys. J.* **94**, L41-L43 (2008).

12. Petrov, Eugene P. & Schwille, P. Correction. *Biophys. J.* **103**, 375 (2012).

13. Horner, A. & Pohl, P. Comment on "Enhanced water permeability and tunable ion selectivity in subnanometer carbon nanotube porins". *Science* **359**, eaap9173 (2018).

14. Verkman, A. S. Development and biological applications of chloride-sensitive fluorescent indicators. *American Journal of Physiology-Cell Physiology* **259**, C375-C388 (1990).

15. Biwersi, J., Tulk, B. & Verkman, A. S. Long-Wavelength Chloride-Sensitive Fluorescent Indicators. *Anal. Biochem.* **219**, 139-143 (1994).

16. Geise, G. M., Park, H. B., Sagle, A. C., Freeman, B. D. & McGrath, J. E. Water permeability and water/salt selectivity tradeoff in polymers for desalination. *J. Membr. Sci.* **369**, 130-138 (2011).

17. Park, H. B., Kamcev, J., Robeson, L. M., Elimelech, M. & Freeman, B. D. Maximizing the right stuff: The trade-off between membrane permeability and selectivity. *Science* **356**, eaab0530 (2017).

18. Berezhkovskii, A. & Hummer, G. Single-File Transport of Water Molecules through a Carbon Nanotube. *Phys. Rev. Lett.* **89**, 064503 (2002).

19. Zhu, F., Tajkhorshid, E. & Schulten, K. Collective Diffusion Model for Water Permeation through Microscopic Channels. *Phys. Rev. Lett.* **93**, 224501 (2004).

20. Tunuguntla, R. H. et al. Enhanced water permeability and tunable ion selectivity in subnanometer carbon nanotube porins. *Science* **357**, 792-796 (2017).

21. Werber, J. R. & Elimelech, M. Permselectivity limits of biomimetic desalination membranes. *Sci. Adv.* **4**, eaar8266 (2018).

22. Humphrey, W., Dalke, A. & Schulten, K. VMD: Visual molecular dynamics. *J. Mol. Graphics Model.* **14**, 33-38 (1996).

23. Vanommeslaeghe, K. et al. CHARMM general force field: A force field for drug-like molecules compatible with the CHARMM all-atom additive biological force fields. *J. Comput. Chem.* **31**, 671-690 (2010).

24. Best, R. B. et al. Optimization of the additive CHARMM all-atom protein force field targeting improved sampling of the backbone ϕ, ψ and side-chain $\chi1$ and $\chi2$ dihedral angles. *J. Chem. Theory Comput.* **8**, 3257-3273 (2012).

25. Chowdhury, R. et al. PoreDesigner for tuning solute selectivity in a robust and highly permeable outer membrane pore. *Nat. Commun.* **9**, 3661 (2018).

26. Entzminger, K. C. et al. De novo design of antibody complementarity determining regions binding a FLAG tetra-peptide. *Sci. Rep.* **7**, 10295 (2017).

27. Latimer, P. & Pyle, B. E. Light Scattering at Various Angles: Theoretical Predictions of the Effects of Particle Volume Changes. *Biophys. J.* **12**, 764-773 (1972).